Continuum Mech. Thermodyn. (2007) 18: 377–394
DOI 10.1007/s00161-006-0032-7

ORIGINAL ARTICLE

Xiaoyu Zheng · M. Gregory Forest · Robert Lipton · Ruhai Zhou

Nematic polymer mechanics: flow-induced anisotropy

Received: 9 June 2006 / Accepted: 9 October 2006 / Published online: 21 December 2006

Abstract In this paper, we model and compute flow-induced mechanical properties of nematic polymer nanocomposites, consisting of transversely isotropic rigid spheroids in an isotropic matrix. Our goal is to fill a gap in the theoretical literature between random and perfectly aligned spheroidal composites (Odegard et al. in Compos. Sci. Technol. **63**, 1671–1687, 2003; Gusev et al. in Adv. Eng. Mater. **4**(12), 927–931 2002; Torquato in Random heterogeneous materials. Springer, Berlin Heidelberg New York, 2002; Milton in The Theory of Composites. Cambridge University Press, Cambridge, 2002) by modeling the influence of nano-particle volume fraction, flow type and flow rate on nano-composite elasticity tensors. As these influences vary, we predict the degree of elastic anisotropy, determining the number of independent moduli, and compute their values relative to the nano-particle and matrix moduli. We restrict here to monodomains, addressing features associated with orientational configurations of the rod or platelet ensemble. The key modeling advance is the transfer of symmetries (Forest et al. in Phys. Fluids **12**(3), 490–498, 2000) and numerical databases (Forest et al. in Rheol. Acta **43**(1), 17–37, 2004a, Rheol. Acta **44**(1), 80–93, 2004b) for the orientational probability distribution function of the nematic polymer ensemble into the classical Mori–Tanaka effective elasticity tensor formalism. Isotropic, transversely isotropic, orthotropic, monoclinic, and maximally anisotropic elasticity tensors are realized as volume fraction, imposed flow type and flow strength are varied, with 2, 5, 9, 13 or 21 independent moduli for the various symmetries.

Keywords Elastic moduli, Nano-rods, Composite properties, Nematics polymer, Flow

PACS 62.20.Dc, 62.25+g

1 Introduction

Nano-elements with high-contrast properties are combined at low (0.1–5%) volume fractions with traditional polymeric materials to enhance a diverse set of targeted properties [29]. Notable examples are high electrical

Communicated by E. Virga

X. Zheng (✉)
Department of Mathematical Sciences, Kent State University, Kent, OH, USA
E-mail: zheng@math.kent.edu

M. G. Forest
Department of Mathematics, University of North Carolina at Chapel Hill, Chapel Hill, NC, USA

R. Lipton
Department of Mathematics, Louisiana State University, Baton Rouge, LA, USA

R. Zhou
Department of Mathematics and Statistics, Old Dominion University, Norfolk, VA, USA

conductivity and strength of carbon-based nano-rods and nano-fibers [20,24] and barrier properties of nano-clay platelets [16]. We have studied the role of orientational distributions of flow-generated nano-rod ensembles on the effective conductivity of such composites by homogenization theory in the low volume fraction limit [12,31]. Our goal here is to extend these predictions to mechanical properties, which are then compared with the extreme limits of random and perfect orientation of the nano-particles. For this paper we assume a rapid quench from the liquid to solid phase which maintains the equilibrium or flow-induced orientational probability distribution function (PDF) of the nano-inclusions.

Composite properties, whether electrical or thermal conductivity, gas or liquid permeability, or elastic moduli, require an appropriate averaging algorithm. Homogenization theory provides a rigorous averaging method in certain well-defined asymptotic limits. The key asymptotic features of nano-rod composites are the low volume fraction and high aspect ratio of the nano-rod particles. The theory also provides a predictive framework based on any known PDF of the nano-rod ensemble. More precisely, second and fourth moments of the PDF uniquely determine the mechanical property tensor, where the low moments can arise from experimental data or models.

For this paper, we use numerical databases for the PDFs of quiescent and flow-induced nano-rod dispersions, acquired by simulations of the Smoluchowski equation of Doi–Hess kinetic theory [9,10]. The application of the Doi–Hess hydrodynamic theory to rigid rod and platelet macromolecules is well established; its applicability to larger particles such as carbon nanotubes is open to scientific debate and inquiry. The Doi–Hess theory was derived for Brownian rods in a viscous solvent, and has an equivalent stochastic differential equation. However, the Smoluchowski equation that results may indeed have wider applicability to particles on a different scale. The physics in the model consists of an excluded-volume potential which captures the isotropic–nematic phase transition of the rod ensemble, and a hydrodynamic contribution from the flow field, which is given by the Jeffery orbit of a spheroid in Stokes flow (a macroscopic effect). Indeed, some evidence that the Doi–Hess hydrodynamic theory has predictive value for a wider range of rod and platelet nano-composites than simply nematic polymer materials is given by the experimentally observed nematic liquid crystallinity of multiwall carbon nanotubes in an aqueous solvent [27]. It is reasonable to assume that excluded volume interactions of the large-aspect-ratio rods are responsible, since the authors report classical hysteresis between isotropic and nematic phases, which is precisely what the theory predicts. The details for such rod dispersions may not be accurately captured by the PDFs of the Doi–Hess theory, but the symmetries and qualitative predictions are likely to be quite valuable in guiding experimental validation of anisotropy in mechanical property tensors. Following our first papers on conductivity of nano-rod composites, we restrict this study to volume fractions and flow rates which yield stable steady distributions. We calculate mechanical properties for rest equilibria, planar shear (using previous numerical solutions) and uniaxial extension (extending previous numerical solutions for extensional flow from second-moment tensor models to the kinetic level).

In Sect. 2, we introduce background information on elasticity tensors and orientation averages which arise in such tensors. In Sect. 3, we derive symmetries of the effective elasticity tensors inherited from PDF symmetries, and then determine the number of independent elastic moduli versus volume fraction and flow type. (This is a tedious exercise in tensor algebra, yet heretofore there is no theoretical guidance to indicate the degree of mechanical anisotropy in rigid rod or platelet composites whose particle PDFs lie between random and perfectly aligned probability distributions.) In Sect. 4, we combine the Mori–Tanaka averaging theory with the PDF databases of Doi–Hess theory to predict quantitative enhancements of all independent mechanical moduli from given nano-phase and matrix properties.

2 Background on elasticity tensors and symmetries

2.1 Stress–strain relations

Throughout the paper, we use Greek letters (e.g. τ, ε) to denote a second-order tensor, capital letters (e.g. C, I, S) to denote a fourth-order tensor, and lower-case letters (e.g. u, t, x) to denote a vector or scalar.

Let $u(x)$ denote the displacement, $\tau(x)$ and $\varepsilon(x)$ denote the symmetric local stress and strain tensors at position x. In steady states without sources, $\tau(x)$ and $\varepsilon(x)$ satisfy [28]:

$$\nabla \cdot \tau(x) = 0, \quad \nabla \times (\nabla \times \varepsilon)^{\mathrm{T}} = 0, \tag{1}$$

which means the strain can be written as a symmetrized gradient of displacements $u(x)$,

$$\varepsilon(x) = \frac{1}{2}\left[\nabla u(x) + \nabla u(x)^{\mathrm{T}}\right]. \tag{2}$$

The linear elastic constitutive law is

$$\tau(x) = C(x) : \varepsilon(x), \quad \varepsilon(x) = M(x) : \tau(x), \tag{3}$$

where the fourth-order tensors C and M are the local stiffness and compliance tensor with

$$C : M = I, \quad I = \frac{1}{2}[\delta_{ik}\delta_{jl} + \delta_{il}\delta_{jk}], \tag{4}$$

and I is the fourth-order identity tensor.

We are concerned here with two-phase composites, consisting of a nano-particle phase of rods or platelets and a matrix phase. Each phase satisfies (1)–(3) with distinct, and often highly contrasted, stiffness tensors. From classical homogenization theory, the composite satisfies a form of (3), but with averaged stress, strain and effective stiffness tensor C^e:

$$\langle \tau(x) \rangle = C^e : \langle \varepsilon(x) \rangle, \tag{5}$$

under the assumption that the phases are perfectly bonded.

2.2 The stiffness tensor and elastic moduli versus symmetry

Since the stress tensor and strain tensor are symmetric, we must have

$$C_{ijkl} = C_{jikl}, \quad C_{ijkl} = C_{ijlk}. \tag{6}$$

This reduces the 81 independent components of C_{ijkl} to 36 for three-dimensional elasticity. It is traditional [28] to retain the label C for the 6×6 matrix representation of these 36 stiffness constants. Likewise, the stress and strain tensors are compressed into six-dimensional vectors so that (3) reduces to:

$$\begin{pmatrix} \tau_1 \\ \tau_2 \\ \tau_3 \\ \tau_4 \\ \tau_5 \\ \tau_6 \end{pmatrix} = \begin{pmatrix} C_{11} & C_{12} & C_{13} & C_{14} & C_{15} & C_{16} \\ C_{12} & C_{22} & C_{23} & C_{24} & C_{25} & C_{26} \\ C_{13} & C_{23} & C_{33} & C_{34} & C_{35} & C_{36} \\ C_{14} & C_{24} & C_{34} & C_{44} & C_{45} & C_{46} \\ C_{15} & C_{25} & C_{35} & C_{45} & C_{55} & C_{56} \\ C_{16} & C_{26} & C_{26} & C_{46} & C_{56} & C_{66} \end{pmatrix} \begin{pmatrix} \varepsilon_1 \\ \varepsilon_2 \\ \varepsilon_3 \\ \varepsilon_4 \\ \varepsilon_5 \\ \varepsilon_6 \end{pmatrix}, \tag{7}$$

with the following identification:

$$\begin{aligned} &\tau_i = \tau_{ii}, \quad \text{for } i = 1, 2, 3, \tau_4 = \tau_{23}, \tau_5 = \tau_{13}, \tau_6 = \tau_{12}, \\ &\varepsilon_i = \varepsilon_{ii}, \quad \text{for } i = 1, 2, 3, \varepsilon_4 = 2\varepsilon_{23}, \varepsilon_5 = 2\varepsilon_{13}, \varepsilon_6 = 2\varepsilon_{12}; \end{aligned} \tag{8}$$

while the identification C_{ijkl} and C_{pq} is:

$$11 \leftrightarrow 1, 22 \leftrightarrow 2, 33 \leftrightarrow 3, 23(32) \leftrightarrow 4, 13(31) \leftrightarrow 5, 12(21) \leftrightarrow 6. \tag{9}$$

If the stress can be expressed as a derivative of the strain energy density function with respect to strain, then the stiffness tensor must additionally have the symmetry

$$C_{ijkl} = C_{klij}, \tag{10}$$

which further reduces the number of independent elastic constants to 21. If certain symmetries exist in the material, this number will be reduced even further as follows.

2.2.1 Monoclinic symmetry

For symmetry with respect to one plane, say the x_1–x_2 plane, the elasticity tensor has 13 independent components:

$$C = \begin{pmatrix} C_{11} & C_{12} & C_{13} & 0 & 0 & C_{16} \\ C_{12} & C_{22} & C_{23} & 0 & 0 & C_{26} \\ C_{13} & C_{23} & C_{33} & 0 & 0 & C_{36} \\ 0 & 0 & 0 & C_{44} & C_{45} & 0 \\ 0 & 0 & 0 & C_{45} & C_{55} & 0 \\ C_{16} & C_{26} & C_{36} & 0 & 0 & C_{66} \end{pmatrix}. \tag{11}$$

As in the general anisotropic case, here pure strain can give rise to a normal stress.

2.2.2 Orthotropic symmetry

For symmetry with respect to three orthogonal planes, or alternately three orthogonal symmetry axes, the elasticity tensor has nine independent components. The elasticity tensor in coordinates aligned with principal material directions is:

$$C = \begin{pmatrix} C_{11} & C_{12} & C_{13} & 0 & 0 & 0 \\ C_{12} & C_{22} & C_{23} & 0 & 0 & 0 \\ C_{13} & C_{23} & C_{33} & 0 & 0 & 0 \\ 0 & 0 & 0 & C_{44} & 0 & 0 \\ 0 & 0 & 0 & 0 & C_{55} & 0 \\ 0 & 0 & 0 & 0 & 0 & C_{66} \end{pmatrix}. \tag{12}$$

It is convenient to relate the elastic components to engineering moduli, respectively called the Young's moduli E_1, E_2, E_3 in the 1-, 2- and 3-directions; Poisson's ratios ν_{12}, ν_{13}, ν_{23}, which are defined by the negative of the transverse strain in the j-direction over the strain in the i-direction when stress is applied in the i-direction, and shear moduli G_{12}, G_{13}, G_{23} in the 1–2, 1–3 and 2–3 planes. The correspondences between the elastic components and engineering moduli are:

$$\begin{aligned} &C_{11} = E_1(1 - (E_3/E_2)\nu_{23}^2)D, \quad C_{12} = (E_2\nu_{12} + E_3\nu_{13}\nu_{23})D, \\ &C_{13} = E_3(\nu_{12}\nu_{23} + \nu_{13})D, \quad C_{22} = E_2(1 - (E_3/E_1)\nu_{13}^2)D, \\ &C_{23} = (E_3/E_1)(E_1\nu_{23} + E_2\nu_{12}\nu_{13})D, \quad C_{33} = E_3(1 - (E_2/E_1)\nu_{12}^2)D, \\ &C_{44} = G_{23}, \quad C_{55} = G_{13}, \quad C_{66} = G_{12}, \end{aligned} \tag{13}$$

with

$$D^{-1} = 1 - 2(E_3/E_1)\nu_{12}\nu_{23}\nu_{13} - \nu_{13}^2(E_3/E_2) - \nu_{23}^2(E_3/E_2) - \nu_{12}^2(E_2/E_1). \tag{14}$$

The compliance tensor M can be expressed in terms of the independent moduli:

$$M = \begin{pmatrix} \frac{1}{E_1} & -\frac{\nu_{21}}{E_2} & -\frac{\nu_{31}}{E_3} & 0 & 0 & 0 \\ -\frac{\nu_{12}}{E_1} & \frac{1}{E_2} & -\frac{\nu_{32}}{E_3} & 0 & 0 & 0 \\ -\frac{\nu_{13}}{E_1} & -\frac{\nu_{23}}{E_2} & \frac{1}{E_3} & 0 & 0 & 0 \\ 0 & 0 & 0 & \frac{1}{4G_{23}} & 0 & 0 \\ 0 & 0 & 0 & 0 & \frac{1}{4G_{13}} & 0 \\ 0 & 0 & 0 & 0 & 0 & \frac{1}{4G_{12}} \end{pmatrix}, \tag{15}$$

with $\frac{\nu_{ij}}{E_i} = \frac{\nu_{ji}}{E_j}$.

2.2.3 Transversely isotropic symmetry

For symmetry with respect to one axis, the elasticity tensor has five independent components. For example, if the symmetry axis is the $x_1 = (1, 0, 0)$ axis, then the stiffness tensor can be expressed by:

$$C = \begin{pmatrix} C_{11} & C_{12} & C_{12} & 0 & 0 & 0 \\ C_{12} & C_{22} & C_{23} & 0 & 0 & 0 \\ C_{12} & C_{23} & C_{22} & 0 & 0 & 0 \\ 0 & 0 & 0 & 1/2(C_{22} - C_{23}) & 0 & 0 \\ 0 & 0 & 0 & 0 & C_{66} & 0 \\ 0 & 0 & 0 & 0 & 0 & C_{66} \end{pmatrix}. \tag{16}$$

The five engineering moduli are longitudinal (E_{L}) and transverse (E_{T}) Young's moduli, transverse bulk modulus (k_{T}), longitudinal (G_{L}) and transverse (G_{T}) shear moduli. The components of the stiffness tensor are traditionally labeled according to:

Axial modulus under an axial strain	$n = C_{11}$
Transverse bulk modulus	$k_{\mathrm{T}} = (C_{22} + C_{23})/2$
Cross modulus	$l = C_{12}$
Longitudinal Young's modulus	$E_{\mathrm{L}} = n - l^2/k_{\mathrm{T}}$
Transverse shear modulus	$G_{\mathrm{T}} = (C_{22} - C_{23})/2$
Longitudinal shear modulus	$G_{\mathrm{L}} = C_{66}$
Poisson ratio	$\nu_{12} = l/(2k_{\mathrm{T}})$

2.2.4 Isotropic symmetry

When the elastic moduli are invariant under coordinate transformations, there are only two independent elastic moduli, and C has the representation

$$C = \begin{pmatrix} C_{11} & C_{12} & C_{12} & 0 & 0 & 0 \\ C_{12} & C_{11} & C_{12} & 0 & 0 & 0 \\ C_{12} & C_{12} & C_{11} & 0 & 0 & 0 \\ 0 & 0 & 0 & 1/2(C_{11} - C_{12}) & 0 & 0 \\ 0 & 0 & 0 & 0 & 1/2(C_{11} - C_{12}) & 0 \\ 0 & 0 & 0 & 0 & 0 & 1/2(C_{11} - C_{12}) \end{pmatrix}, \tag{17}$$

where $C_{12} = \lambda$ is the Lamé constant, $1/2(C_{11} - C_{12}) = G$ is the shear modulus, and $K = \lambda + \frac{2}{3}G$ is the bulk modulus governing volumetric and dilatational changes. The isotropic elasticity and compliance tensors can also be expressed using indicial notation:

$$\begin{aligned} C_{ijkl} &= \left(K - \frac{2}{3}G\right)\delta_{ij}\delta_{kl} + G(\delta_{ik}\delta_{jl} + \delta_{il}\delta_{jk}), \\ M_{ijkl} &= \left(\frac{1}{9K} - \frac{1}{6G}\right)\delta_{ij}\delta_{kl} + \frac{1}{4G}(\delta_{ik}\delta_{jl} + \delta_{il}\delta_{jk}). \end{aligned} \tag{18}$$

The relationships between the shear modulus G, Young's modulus E, bulk modulus K, and transverse bulk modulus k_T are given by

$$G = \frac{E}{2(1+\nu)}, \quad K = \frac{E}{3(1-2\nu)}, \quad k_{\mathrm{T}} = K + G/3. \tag{19}$$

2.3 Mori–Tanaka theory for the effective stiffness tensor

Considering a perfect bond between the inclusions and matrix, the effective stiffness tensor of a dilute (low volume fraction θ_2) suspension is given by Hill [19]:

$$C^e = C_1 + \theta_2\langle N\rangle + O(\theta_2^2), \tag{20}$$

$$N = (C_2 - C_1) : T, \quad T = [I + S : C_1^{-1} : (C_2 - C_1)]^{-1}, \quad \langle\cdot\rangle = \int_{S^2} \cdot\, f\, d\mathbf{m}, \tag{21}$$

where C_1 and C_2 are stiffness tensors for the matrix and inclusion; S is the Eshelby tensor for an ellipsoidal inclusion embedded in an isotropic matrix with Poisson ratio ν_1; N is the polarization tensor, T is the Wu strain tensor (cf. [28]), and f is the orientational PDF of the inclusions.

The effective stiffness tensor for composites approximated by Mori–Tanaka theory is given by

$$C^e = C_1 + \theta_2\langle N\rangle : (\theta_1 I + \theta_2\langle T\rangle)^{-1}, \tag{22}$$

which purports to account for interactions between the inclusions and matrix and is assumed to be valid for any volume fraction θ_2.

The computation of the tensor C^e is straightforward yet tedious. Since S and C_2 are transversely isotropic, and C_1 is isotropic, we can use standard rules for the inner products of tensors given below in Sect. 2.5.

2.4 Eshelby tensor S

For a spheroidal inclusion embedded in a matrix with Poisson ratio ν_1, and aspect ratio $\alpha = a/b$, the Eshelby tensor S is given by [4]:

$$
\begin{aligned}
S_{2222} &= S_{3333} = \frac{3}{8(1-\nu_1)}\frac{\alpha^2}{\alpha^2-1} + \frac{1}{4(1-\nu_1)}\left[1-2\nu_1 - \frac{9}{4(\alpha^2-1)}\right]q,\\
S_{1111} &= \frac{1}{2(1-\nu_1)}\left\{1-2\nu_1 + \frac{3\alpha^2-1}{\alpha^2-1} - \left[1-2\nu_1+\frac{3\alpha^2}{\alpha^2-1}\right]q\right\},\\
S_{3322} &= S_{2233} = \frac{1}{4(1-\nu_1)}\left\{\frac{\alpha^2}{2(\alpha^2-1)} - \left[1-2\nu_1+\frac{3}{4(\alpha^2-1)}\right]q\right\},\\
S_{3311} &= S_{2211} = \frac{1}{2(1-\nu_1)}\left\{\frac{-\alpha^2}{\alpha^2-1} + \frac{1}{2}\left[\frac{3\alpha^2}{\alpha^2-1} - (1-2\nu_1)\right]q\right\},\\
S_{1133} &= S_{1122} = \frac{1}{2(1-\nu_1)}\left\{2\nu_1 - 1 - \frac{1}{\alpha^2-1} + \left[1-2\nu_1+\frac{3}{2(\alpha^2-1)}\right]q\right\},\\
S_{2323} &= \frac{1}{4(1-\nu_1)}\left\{\frac{\alpha^2}{2(\alpha^2-1)} + \left[1-2\nu_1-\frac{3}{4(\alpha^2-1)}\right]q\right\},\\
S_{1212} &= S_{1313} = \frac{1}{4(1-\nu_1)}\left\{1-2\nu_1 - \frac{\alpha^2+1}{\alpha^2-1} - \frac{1}{2}\left[1-2\nu_1-\frac{3(\alpha^2+1)}{(\alpha^2-1)}\right]q\right\}.
\end{aligned}
\tag{23}
$$

$$
q = \begin{cases} \dfrac{\alpha}{(\alpha^2-1)^{3/2}}[\alpha(\alpha^2-1)^{1/2} - \cosh^{-1}\alpha], & \alpha \geq 1,\\[2ex] \dfrac{\alpha}{(1-\alpha^2)^{3/2}}[\cos^{-1}\alpha - \alpha(\alpha^2-1)^{1/2}], & \alpha \leq 1. \end{cases}
\tag{24}
$$

Since S is not symmetric (except for a sphere in an isotropic matrix), S can be expressed following the classical notation [19,30]:

$$
S = (S_{2222} + S_{2233},\, S_{1122},\, S_{2211},\, S_{1111},\, 2S_{2323},\, 2S_{1212}),
\tag{25}
$$

specialized to a spheroid.

2.5 Tensor computations

We follow the notation in [19] for transversely isotropic tensors:

$$
C_2 = (2k_T, l, l, n, 2G_T, 2G_L).
\tag{26}
$$

With this notation, the tensor operations yield (cf. [26]):

$$
\begin{aligned}
C &= (c, g, h, d, e, f), \quad C' = (c', g', h', d', e', f'),\\
C\,M &= I, \quad I = (1, 0, 0, 1, 1, 1),\\
M &= (d/(cd-2gh), -g/(cd-2gh), -h/(cd-2gh), c/(cd-2gh), 1/e, 1/f),\\
CC' &= (cc' + 2hg', gc' + dg', hd' + ch', dd' + 2gh', ee', ff'),
\end{aligned}
\tag{27}
$$

where M is again the compliance tensor.

For an isotropic stiffness tensor (which will be specified for the matrix, where we attach the subscript 1), following the same notation and operations, we have

$$
\begin{aligned}
C_1 &= (2k_1, l_1, l_1, n_1, 2G_1, 2G_1) = (2(K+1/3G), K-2/3G, K-2/3G, K+4/3G, 2G, 2G),\\
M_1 &= \left(\frac{1-\nu_1}{E_1}, -\frac{\nu_1}{E_1}, -\frac{\nu_1}{E_1}, \frac{1}{E_1}, \frac{1}{2G}, \frac{1}{2G}\right).
\end{aligned}
\tag{28}
$$

We now provide the result of computation of T and N from Eq. (21):

$$
\begin{aligned}
P = S : C_1^{-1} &= \Bigg(\frac{1}{E_1}[(1-\nu_1)(S_{2222}+S_{2233}) - 2\nu_1 S_{2211}],\ \frac{1}{E_1}[(1-\nu_1)S_{1122} - \nu_1 S_{1111}], \\
&\qquad \frac{1}{E_1}(S_{2211} - \nu_1(S_{2222}+S_{2233})),\ \frac{1}{E_1}(S_{1111} - 2\nu_1 S_{1122}),\ \frac{1}{G_1}S_{2323},\ \frac{1}{G_1}S_{1212}\Bigg), \\
[I + P : (C_2 - C_1)] &= (c', g', h', d', e', f'), \\
c' &= 1 + \frac{2(k_2-k_1)}{E_1}[(1-\nu_1)(S_{2222}+S_{2233}) - 2\nu_1 S_{2211}] + \frac{2(l_2-l_1)}{E_1}[S_{2211} - \nu_1(S_{2222}+S_{2233})], \\
d' &= 1 + \frac{n_2-n_1}{E_1}[S_{1111} - 2\nu_1 S_{1122}] + \frac{2(l_2-l_1)}{E_1}[(1-\nu_1)S_{1122} - \nu_1 S_{1111}], \\
e' &= 1 + \frac{2(G_T - G_1)}{G_1}S_{2323}, \\
f' &= 1 + \frac{2(G_L - G_1)}{G_1}S_{1212}, \\
g' &= \frac{2(k_2-k_1)}{E_1}[(1-\nu_1)S_{1122} - \nu_1 S_{1111}] + \frac{l_2-l_1}{E_1}[S_{1111} - 2\nu_1 S_{1122}], \\
h' &= \frac{n_2-n_1}{E_1}[S_{2211} - \nu_1(S_{2222}+S_{2233})] + \frac{l_2-l_1}{E_1}[(1-\nu_1)(S_{2222}+S_{2233}) - 2\nu_1 S_{2211}].
\end{aligned} \tag{29}
$$

$$
\begin{aligned}
T &= [I + P : (C_2 - C_1)]^{-1} = (d'/p', -g'/p', -h'/p', c'/p', 1/e', 1/f'), \quad p' = c'd' - 2g'h', \\
N &= (C_2 - C_1) : T = (c, g, h, d, e, f), \\
c &= 2(k_2-k_1)d'/p' - 2(l_2-l_1)g'/p', \\
g &= (l_2-l_1)d'/p' - (n_2-n_1)g'/p', \\
h &= (l_2-l_1)c'/p' - 2h'(k_2-k_1)/p', \\
d &= (n_2-n_1)c'/p' - 2h'(l_2-l_1)/p', \\
e &= 2(G_T - G_1)/e', \\
f &= 2(G_L - G_1)/f'.
\end{aligned} \tag{30}
$$

To complete the Mori–Tanaka formula, all that remains is the orientational average of T and N, Eq. (22). This is the object of the next section.

2.6 Orientational averages

To compute orientational averages of the fourth-order tensors enclosed within angle brackets in Eq. (22), we need to transform local coordinates (x, y, z) to global coordinates (x', y', z'). This change of coordinates is given by

$$
\bar{N}_{ijkl} = \omega_{ip}\omega_{jq}\omega_{kr}\omega_{ls}N_{pqrs}, \tag{31}
$$

where the components of ω_{ij} are the direction cosines for the transformation of Euler angles:

$$
\omega(\phi, \theta, \psi) = \begin{pmatrix} \cos\phi & \sin\phi & 0 \\ -\sin\phi & \cos\phi & 0 \\ 0 & 0 & 1 \end{pmatrix} \begin{pmatrix} \cos\theta & 0 & \sin\theta \\ 0 & 1 & 0 \\ -\sin\theta & 0 & \cos\theta \end{pmatrix} \begin{pmatrix} \cos\psi & \sin\psi & 0 \\ -\sin\psi & \cos\psi & 0 \\ 0 & 0 & 1 \end{pmatrix}. \tag{32}
$$

Using this coordinate transformation, the averaging operation $\langle N \rangle$ becomes:

$$
\langle N \rangle = \frac{\int_0^{\pi}\int_0^{\pi/2}\int_0^{\pi} \bar{N}(\phi, \theta, \psi) f(\phi, \theta, \psi) \sin\theta \, \mathrm{d}\phi \, \mathrm{d}\theta \, \mathrm{d}\psi}{\int_0^{\pi}\int_0^{\pi/2}\int_0^{\pi} f(\phi, \theta, \psi) \sin\theta \, \mathrm{d}\phi \, \mathrm{d}\theta \, \mathrm{d}\psi}. \tag{33}
$$

However, the above integral is difficult to compute, so we proceed as follows. If N is a rank 4 transversely isotropic tensor, it has the six-vector representation described earlier, $N = (c, g, h, d, e, f)$. Alternatively, N

can be represented as a linear combination of the six-dimensional basis of transversely isotropic tensors, with **m** a unit vector corresponding to the axis of symmetry of N,

$$\begin{aligned} N_{ijkl}(\mathbf{m}) = {} & b_1 m_i m_j m_k m_l + b_2(\delta_{ik} m_j m_l + \delta_{il} m_j m_k + \delta_{jk} m_i m_l + \delta_{jl} m_i m_k) \\ & + b_3 \delta_{ij} m_k m_l + b_4 \delta_{kl} m_i m_j + b_5 \delta_{ij} \delta_{kl} + b_6(\delta_{ik}\delta_{jl} + \delta_{il}\delta_{jk}), \end{aligned} \tag{34}$$

and the relationship between these two *coordinates* of N is

$$\begin{aligned} & b_1 = d + (c+e)/2 - g - h - 2f, \quad b_2 = (f-e)/2, \\ & b_3 = h - (c-e)/2, \quad b_4 = g - (c-e)/2, \\ & b_5 = (c-e)/2, \quad b_6 = e/2. \end{aligned} \tag{35}$$

(Note: The developments above assume (Eq. 10), which forces $b_3 = b_4$, and thus there are five independent elements of transversely isotropic N.)

We denote the second moment $\mathbf{M}_2$ and fourth moment $\mathbf{M}_4$ of the PDF f by:

$$\mathbf{M}_2 = \langle m_i m_j \rangle, \quad \mathbf{M}_4 = \langle m_i m_j m_k m_l \rangle. \tag{36}$$

The orientational average of a transversely isotropic tensor N is therefore given by:

$$\begin{aligned} \langle N \rangle = {} & b_1 \mathbf{M}_4 + b_2(\delta_{ik} M_{jl} + \delta_{il} M_{jk} + \delta_{jk} M_{il} + \delta_{jl} M_{ik}) \\ & + b_3 \delta_{ij} M_{kl} + b_4 \delta_{kl} M_{ij} + b_5 \delta_{ij}\delta_{kl} + b_6(\delta_{ik}\delta_{jl} + \delta_{il}\delta_{jk}), \end{aligned} \tag{37}$$

where M_{ij} denotes the corresponding components of $\mathbf{M}_2$. We note that Doi–Hess kinetic theory of nematic polymers provides the PDF f of the inclusions, from which fourth and second moments are given by projection onto the first several terms in a spherical harmonic expansion [9,10]. Traditional Landau–deGennes or second-moment tensor models only provide $\mathbf{M}_2$, and some additional *ad hoc* rule has to be invoked to get the fourth moment $\mathbf{M}_4$.

3 A hierarchy of symmetries of the effective elasticity tensor of nano-rod composites

The orientational distributions of nano-elements often possess certain symmetries. Armed with the above developments, we now show how particle symmetries and mean-field PDF symmetries can be combined to prove symmetries of the effective elasticity and compliance tensors of the nano-composites. These symmetry results then provide a rigorous determination of the number of independent components of C^e, which is identical to the number of independent elastic moduli (or elasticity constants); subsequently, we compute the value of each modulus and confirm the symmetries.

Recall that C_1 is an isotropic tensor and C_2 is a transversely isotropic tensor.

1. **Random distribution limit:** *C^e is isotropic with two independent components (and elastic moduli).* In the dilute limit, the PDF f is isotropic at rest, which implies

$$\mathbf{M}_2 = \frac{1}{3}\delta_{ij}, \quad \mathbf{M}_4 = \frac{1}{15}(\delta_{ij}\delta_{kl} + \delta_{ik}\delta_{jl} + \delta_{il}\delta_{jk}). \tag{38}$$

From Eq. (37), we get $\langle N \rangle$ explicitly for random orientational distributions:

$$\langle N \rangle_{ijkl} = \left(b_5 + \frac{1}{15}b_1 + \frac{1}{3}(b_3 + b_4)\right)\delta_{ij}\delta_{kl} + \left(b_6 + \frac{1}{15}b_1 + \frac{2}{3}b_2\right)(\delta_{ik}\delta_{jl} + \delta_{il}\delta_{jk}). \tag{39}$$

which is, of course, isotropic. The same argument shows that $\langle T \rangle$, Eq. (21), is also isotropic. Further, since inversion, summation, and contraction preserve isotropy, the composite elasticity tensor C^e, Eq. (22), is isotropic.

2. **Perfect alignment limit:** *C^e is transversely isotropic with five independent components (and elastic moduli).* Although not physically realizable, the extreme limit of perfect particle alignment across the entire ensemble is often considered. Mathematically, this limit allows exact analysis, and it is widely believed to represent some form of extreme bound, with the random alignment limit at the other extreme. (We will investigate these limits in examples to follow; it will turn out that moduli do not always lie between these limits.) Suppose all particles have the identical direction $\mathbf{m} = (m_1, m_2, m_3)$, so the PDF f is a delta distribution:
$$f(\mathbf{m}) = \delta(\mathbf{m}). \tag{40}$$
Using Eq. (33), $\langle N\rangle_{ijkl} = N_{ijkl}(\mathbf{m})$. From Eq. (22), the effective stiffness tensor C^e has the form Eq. (34), which by construction is transversely isotropic, with principal axis $\mathbf{m}$.
3. **Biaxial PDFs generated by rotational flow:** *C^e are maximally anisotropic with 21 independent components (and elastic moduli).* Under simple shear or other rotational flows, the PDFs are generically biaxial, i.e., the second moment $\mathbf{M}_2$ has five independent components. Since C^e inherits the symmetries of $\mathbf{M}_4$ and $\mathbf{M}_2$, we proceed to properties of $\mathbf{M}_4$.
Generally, without any known symmetries, the fourth moment $\mathbf{M}_4$ of the orientational distribution is symmetric under all permutations of subscripts, i.e., $\mathbf{M}_{ijkl} = \mathbf{M}_{jikl} = \mathbf{M}_{klij} = \mathbf{M}_{lijk} = \mathbf{M}_{kijl}$. These conditions reduce the number of independent components of $\mathbf{M}_4$ from 81 to 15. Furthermore, there are additional orthogonality relations between $\mathbf{M}_4$ and $\mathbf{M}_2$,
$$\sum_k \mathbf{M}_{ijkk} = \mathbf{M}_{ij}, \quad \sum_i \mathbf{M}_{ii} = 1. \tag{41}$$
These relations imply that, *if* one knows $\mathbf{M}_2$, then six components of $\mathbf{M}_4$ can be constructed. Thus, the number of independent elements of $\mathbf{M}_4$, given $\mathbf{M}_2$, is nine, which coincides with the space of orthotropic rank 4 tensors; however this is indeed a coincidence, in that $\mathbf{M}_4$ is *not necessarily orthotropic*. Any orthotropic rank 4 tensor has the form of (12) in some orthogonal frame; if $\mathbf{M}_4$ is orthotropic, the orthogonal symmetry axes that yield the representation (12) come from the orthogonal frame of $\mathbf{M}_2$.
Faraoni et al. [5] showed numerically that $\mathbf{M}_4$ in shear flow does not obey orthotropic symmetry, as we have explained above. The elasticity tensor for shear flow is, in general, maximally anisotropic, with 21 independent moduli. For special PDFs which obey in-plane symmetry with respect to the shear flow plane, then $\mathbf{M}_4$ inherits symmetry with respect to the flow plane. PDFs of this type include in-plane steady states, tumbling and wagging orbits, and logrolling steady states. For these PDFs, $\mathbf{M}_4$ has *monoclinic symmetry*. All simulations below confirm this property. For out-of-plane monodomain attractors, e.g. kayaking limit cycles, out-of-plane steady states, and chaotic orbits, $\mathbf{M}_4$ has no a priori special symmetry.
4. **Biaxial PDFs generated by irrotational flow:** *C^e is orthotropic with nine independent components* (*and elastic moduli*). For triaxial extensional flow, or for coplanar shear and extra magnetic fields, the PDFs are generally biaxial [13,14].
For any irrotational flow, the steady-state orientational distribution function is given by a Boltzmann distribution with potential $V(\mathbf{m})$ [1,13,14,25]
$$f(\mathbf{m}) = \frac{1}{Z}\mathrm{e}^{-V(\mathbf{m})}, \quad Z = \int\limits_{|\mathbf{m}|=1} \mathrm{e}^{-V(\mathbf{m})}\mathrm{d}\mathbf{m}, \tag{42}$$
where
$$V(\mathbf{m}) = -\frac{3N}{2}\mathbf{M}_2 : \mathbf{mm} + \frac{1}{2}D_e : \mathbf{mm}; \tag{43}$$
the second moment $\mathbf{M}_2$, because it has trace 1 and is symmetric, has the spectral representation:
$$\mathbf{M}_2 = \sum_{i=1}^{3} d_i \mathbf{n}_i, \quad 0 \le d_3 \le d_2 \le d_1 \le 1, \quad \sum d_i = 1, \tag{44}$$
and an equivalent order parameter representation,
$$\mathbf{M}_2 = s\left(\mathbf{n}_1\mathbf{n}_1 - \frac{\mathbf{I}}{3}\right) + \beta\left(\mathbf{n}_2\mathbf{n}_2 - \frac{\mathbf{I}}{3}\right) + \frac{\mathbf{I}}{3}, \tag{45}$$

where $s = d_1 - d_3$ is the Flory order parameter, and $\beta = d_2 - d_3$ is the biaxiality parameter; with diagonal rate of strain tensor D_e,

$$D_e = \text{diag}(x, y, z), \quad \text{with } x + y + z = 0. \tag{46}$$

If we parameterize the unit vector $\mathbf{m}$ by

$$\mathbf{m} = \cos\theta\, \mathbf{n}_1 + \sin\theta\cos\phi\, \mathbf{n}_2 + \sin\theta\sin\phi\, \mathbf{n}_3, \tag{47}$$

then we can rewrite $V(\mathbf{m})$ in spherical coordinates θ and ϕ,

$$V(\mathbf{m}) = -\frac{3N}{2}\left((s - \beta/2)\cos^2\theta + \frac{\beta}{2}\sin^2\theta\cos 2\phi\right) + \frac{1}{2}\left(x\cos^2\theta + (y\cos^2\phi + z\sin^2\phi)\sin^2\theta\right). \tag{48}$$

Without loss of generality, we take $\mathbf{n}_1 = (1, 0, 0)^{\mathrm{T}}, \mathbf{n}_2 = (0, 1, 0)^{\mathrm{T}}$. By the definition of $\mathbf{M}_4$, we can easily show that $\mathbf{M}_{ii12}, \mathbf{M}_{ii13}, \mathbf{M}_{ii23}, (i = 1, 2, 3)$ are zero, which proves that $\mathbf{M}_4$ is orthotropic and the *effective stiffness tensor* C^e is also *orthotropic*, and the symmetry axes of $\mathbf{M}_4$, C, $\mathbf{M}_2$ are orthogonal and coincident.

5. **Uniaxial PDFs generated at rest and by uniaxial extensional flow:** *C^e is transversely isotropic with five independent components* (*and elastic moduli*). Uniaxial orientational distributions occur at rest above a critical volume fraction, the so-called nematic phase [3,15], in response to uniaxial extensional flow [6, 7,11] and in applied magnetic fields [13], at all volume fractions.
If the PDF is uniaxial, then the fourth moment $\mathbf{M}_4$ is transversely isotropic with $\mathbf{M}_{2222} = \mathbf{M}_{3333}$, $\mathbf{M}_{1122} = \mathbf{M}_{1133}$, so the effective stiffness tensor C^e is transversely isotropic.

4 Mechanical property predictions

In this section, the moduli of nano-rod composites, as predicted using the Mori–Tanaka theory just described, are presented in terms of volume fraction, shear rate, and uniaxial extension rate. These processing conditions, together with particle aspect ratio, parameterize the Doi–Hess kinetic equation for the nano-particle PDF f. We consider typical model nano-rod composites with aspect ratio $r = 100$. So that our predictions have contact with realistic materials, elastic constants of individual transversely isotropic nano-particles (PmPV) in an isotropic matrix, LaRC-SI, are provided in Table 1, adopted from [24]. The longitudinal and transverse Young's moduli of the nano-fibers are 120 and 3.2 times that of the matrix, respectively; the longitudinal and transverse shear moduli are 20 and 3.2 times that of the matrix. The orientational distribution functions are obtained from numerical simulations of the Smoluchowski equation of Doi and Hess [2,9,10,18]. The fundamental objects of interest are:

- nano-rod composite enhancements in moduli relative to the nano-particle/matrix contrasts;
- nonlinear (superlinear) gains which might be exploited in design strategies; and
- anisotropy characterization (number and values of independent elastic moduli).

Table 1 Properties of matrix and nano-rod inclusion(GPa)

Inclusion		Matrix	
k_2	9.9	k_1	6.79
l_2	8.4	l_1	5.43
n_2	457.6	n_1	8.14
G_T	4.4	G_1	1.36
G_L	27.0	G_1	1.36
E_L	450.4	E_1	3.80
E_T	12.1	E_1	3.80
ν_2	0.42	ν_1	0.4

4.1 Effective properties versus volume fraction for quiescent mesophases

First, the relative enhancement of effective moduli (and the number of distinct moduli) are presented as a function of inclusion volume fraction for quiescent phases. Recall the equilibrium phase diagram of nematic polymers exhibits a first-order phase transition and hysteresis in the PDF versus volume fraction (cf. [3]); this feature is described in terms of the Flory order parameter, $s = d_1 - d_3$, computed from the second moment $\mathbf{M}_2(f)$, Fig. 1a. All symmetries of C^e follow from those of $\mathbf{M}_2(f)$, $\mathbf{M}_4(f)$, and corresponding independent moduli are computed from our numerical databases of f, $\mathbf{M}_2$, $\mathbf{M}_4$, according to the above developments and presented in Fig. 1.

We define the relative enhancement of Young's moduli as

$$\mathcal{E}_E = \frac{E^e - E_1}{E_1}, \tag{49}$$

where E^e and E_1 are the effective (composite) and matrix Young modulus, respectively. For other moduli, the relative enhancements are defined similarly.

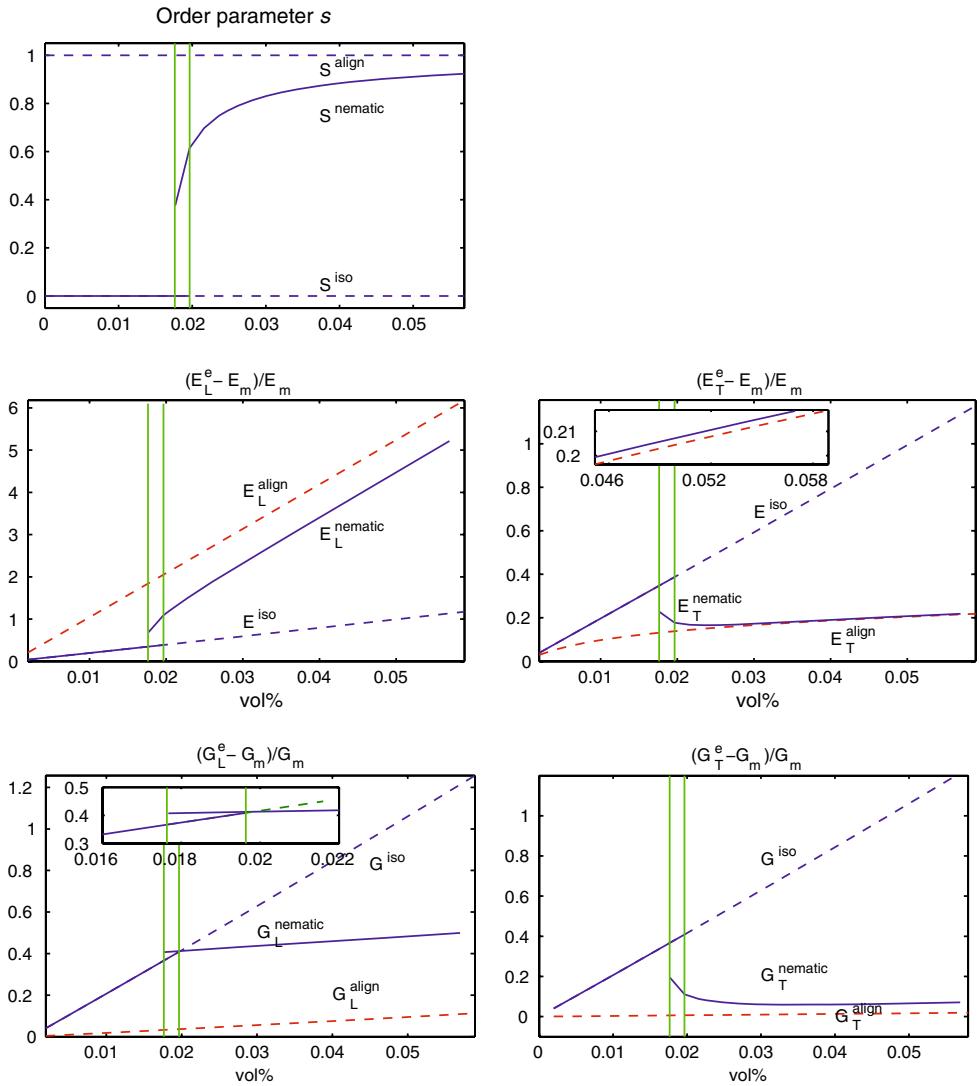

Fig. 1 Volume fraction variability of pure rest phases of aspect ratio 100 particles: **a** order parameter s versus volume fraction θ_2; **b** relative enhancement of longitudinal Young's modulus E^e_L; **c** relative enhancement of transverse Young's modulus E^e_T; **d** relative enhancement of longitudinal shear moduli G^e_L; **e** relative enhancement of transverse shear moduli G^e_T. *Solid curves* are moduli for realistic PDFs, while *dashed curves* are the presumptive extreme bounds generated by perfectly aligned and random PDFs

At sufficiently low volume fractions, $\theta_2 < 1.76\%$ for this specific rod–solvent dispersion, the unique stable equilibrium phase is isotropic: $f(\mathbf{m}) = \dfrac{1}{4\pi}$, $\mathbf{M}_2 = \mathbf{I}/3$, and $s = 0$. For $1.76\% < \theta_2 < 1.96\%$, bi-stable phases coexist, the isotropic phase and an ordered (nematic) equilibrium; for $\theta_2 > 1.96\%$, the nematic phase is the unique stable state. The PDF for nematic equilibria is *uniaxial*, with second moment orientation tensor $\mathbf{Q} = \mathbf{M}_2 - \dfrac{1}{3}\mathbf{I}$ of the form $s(\mathbf{nn} - \mathbf{I}/3)$, where $\mathbf{n}$ is the uniaxial director, and the Flory order parameter s measures the degree of anisotropy.

From the symmetries derived earlier, C^e is *isotropic for isotropic* PDFs, and *transversely isotropic for uniaxial* PDFs, *thus possessing two and five distinct moduli, respectively*. These are simply labeled E^{iso} and G^{iso} in the isotropic phase, while in the nematic phase, the labels are E_L^{nematic} along the principal axis; E_T^{nematic} transverse to the principal axis; G_L^{nematic} on the planes containing the principal axis, G_T^{nematic} on the plane transverse to the principal axis. Values of all moduli in the perfect and random alignment limits are shown for comparison with realistic PDFs.

Fig. 1 conveys that for quiescent phases, *moduli inherit the hysteresis and bistability of the PDF*. There are discontinuous jumps in moduli at the critical volume fraction $\theta_2^* = 1.76\%$, where the nematic phase begins, and $\theta_2^{**} = 1.96\%$, where the isotropic phase becomes unstable.

Young's moduli Figure 1b,c.

Isotropic rest phases E^{iso} increases linearly with volume fraction θ_2, since $f \equiv 1/(4\pi)$ for all θ_2. The line is extended for $\theta_2 > 1.96\%$ to show the contrast with distinct moduli $E_{L,T}^{\text{nematic}}$ of the nematic phase.

Nematic rest phases

- The *longitudinal Young's modulus* E_L^{nematic}, with respect to the coincident principal axis of f, $\mathbf{M}_4$, $\mathbf{M}_2$ and C^e, experiences nonlinear growth as a result of focusing of the rod ensemble along the principal axis (Fig. 1b).
  1. The perfect alignment limit, $s = 1$, yields an *upper bound*, E_L^{align}, shown ranging between 204 and 618% for $1.76\% < \theta_2 < 5.89\%$. By comparison, the composite E_L^{nematic} ranges from 68% to 521% over the same range of volume fractions.
  2. In the bistable range, the nematic phase has 1.8 times greater E_L^e at θ_2^*, increasing to 2.8 times greater E_L^e at θ_2^{**}, again a reflection of nonlinear gain.
- The *transverse Young's modulus* E_T^{nematic}, applies to any direction in the plane normal to the principal symmetry axis $\mathbf{n}_1$ (Fig. 1c), and has the following properties:
  1. E_T^{nematic} lies below the random configuration and above the perfect alignment limit, by symmetry arguments, owing to the number of rods on average available to resist compression or tension in that plane.
  2. E_T^{nematic} decreases to a minimal at $\theta_2 = 2.4\%$, since the PDF becomes more focused, and then slowly converges onto the lower bound of E_T^{align} set by the perfect alignment limit as increasing volume fraction θ_2.
- The Young's moduli together indicate strong anisotropy, with average values

$$E_L^{\text{nematic}} \approx 5.2E_T^{\text{nematic}}, \quad E_T^{\text{nematic}} \approx 1.2E_m. \tag{50}$$

and obey the following order:

$$E_L^{\text{align}} \gg E_L^{\text{nematic}} \gg E^{\text{iso}} > E_T^{\text{nematic}} > E_T^{\text{align}}. \tag{51}$$

Shear moduli Figure 1d,e (We use the following notation for effective longitudinal and transverse shear moduli: $G_L^{\text{nematic}} = G_{12}^e = G_{13}^e$, $G_T^{\text{nematic}} = G_{23}^e$.)

Isotropic rest phases $G^{\text{iso}} = G_L^{\text{iso}} = G_T^{\text{iso}}$, which increase linearly with volume fraction θ_2.

Nematic rest phases

- *The longitudinal shear modulus* G_L^{nematic} (where the peak axis of the PDF defines the longitudinal direction), Fig. 1d.
  1. A distinct longitudinal shear modulus G_L^{nematic} emerges at the onset of the nematic phase, $\theta_2^* = 1.76\%$, with $G_L^{\text{nematic}} = 40.7\%$, which then grows very slowly to 49.9% at $\theta_2 = 5.9\%$. Near θ_2^*, $G_L^{\text{nematic}} > G_L^{\text{iso}}$, this behavior is consistent with [22], who argued that the longitudinal shear modulus obtains a maximum when inclusions are slightly aligned.
  2. $G_L^{\text{align}} \ll G_L^{\text{nematic}} < G_L^{\text{iso}}$ for $\theta_2 > \theta_2^{**}$, since rods tilted towards the longitudinal axis contribute less resistance to shear deformation.
- As the PDF focuses, fewer rods are aligned in transverse planes to the principal axis, thus the *transverse shear modulus* G_T^{nematic} decreases rather quickly towards G_T^{align} (where no rods are aligned in planes transverse to the principal axis), Fig. 1e.

4.2 Effective moduli of flow-induced nano-rod composites

Next, we explore the effect of flow-induced orientational distributions on effective moduli, which typically break isotropic and uniaxial symmetry of the PDFs. By arguments given earlier, C^e is monoclinic symmetric for in-plane sheared PDFs, with 13 independent components, and C^e is orthotropic symmetric for extensional flow with five independent components. We choose the same nano-rod composite properties of Table 1.

First, we fix the inclusions at an *isotropic* volume fraction 1% ($N = 2.54$), and retain the rod aspect ratio at 100. The orientational distributions f are obtained from kinetic theory simulations for a range of shear rates, which yield $\mathbf{M}_2$, $\mathbf{M}_4$ and thereby C^e. All sheared PDFs shown are steady states.

The principal values of the second moment $\mathbf{M}_2$ versus normalized shear rate (Peclet number Pe) are shown in Fig. 2a; recall $d_1 - d_2$ measures anisotropy, while $d_2 - d_3$ measures biaxiality or anisotropy in the plane transverse to the principal axis. We emphasize that $d_1 = d_2 = d_3 = 1/3$ at $Pe = 0$, so all anisotropy arises due to shear flow.

Young's moduli Figure 2b: The enhancements in the distinct Young moduli $E_i^{\text{shear}} (i = 1, 2, 3)$ are shown with respect to the three orthogonal axes of $\mathbf{M}_2$.

1. The largest modulus, E_1^{shear}, associated with the principal axis $\mathbf{n}_1$ ($\mathbf{M}_2$), exhibits nonlinear gain from the shear-induced order, departing from random aligned modulus E^{iso} at $Pe = 0$ and slowly approaching the the upper bound given by E_L^{align}: $E_1^{\text{iso}} < E_1^{\text{shear}} < E_L^{\text{align}}$.
2. The transverse Young's moduli E_2^{shear} and E_3^{shear} fall from E^{iso} for $Pe > 0$, and converge to the lower bound provided by E_T^{align}: $E_T^{\text{align}} < E_3^{\text{shear}} < E_2^{\text{shear}} < E^{\text{iso}}$.

Shear moduli Figure 2c

1. $G_{12}^{\text{shear}} \gg G_{13}^{\text{shear}} > G_{23}^{\text{shear}}$.
2. $G_{12}^{\text{shear}} > G^{\text{iso}} \gg G_L^{\text{align}} > G_T^{\text{align}}$.
3. $G^{\text{iso}} > G_{13}^{\text{shear}} > G_{23}^{\text{shear}} \gg G_L^{\text{align}} > G_T^{\text{align}}$.
4. All shear moduli enhancements are between 10% and 25%, so the gain is not dramatic.

Second, we shift to a concentrated dispersion, $\theta_2 = 2.3\%$ (corresponding to $N = 6$). For this volume fraction, shear once again induces steady PDFs [9,10], called *logrolling states* [21], where the peak axis of f is along the vorticity axis, orthogonal to the shear plane. These PDFs have symmetry with respect to the shear plane, therefore yield monoclinic C^e.

Fig. 3 shows the enhancements of moduli for these logrolling PDFs. Fig. 3a shows $d_1 \gg d_2 \approx d_3$, so the PDF is *weakly biaxial*, and the Young's moduli exhibits nearly uniaxial properties: $E_1^{\text{shear}} \gg E_2^{\text{shear}} \approx E_3^{\text{shear}}$, Fig. 3b,c. The shear moduli obey $G_{12}^{\text{shear}} > G_{13}^{\text{shear}} \gg G_{23}^{\text{shear}}$, with strong contrasts at higher Pe, Fig. 3d,e.

Third, we consider uniaxial extensional flow-induced nano-rod composites at an isotropic volume fraction 1%. Fig. 4a shows $d_1 \gg d_2 = d_3$, so the PDF is uniaxial. Figs. 4b–e show the enhancement of elastic moduli for these uniaxial PDFs.

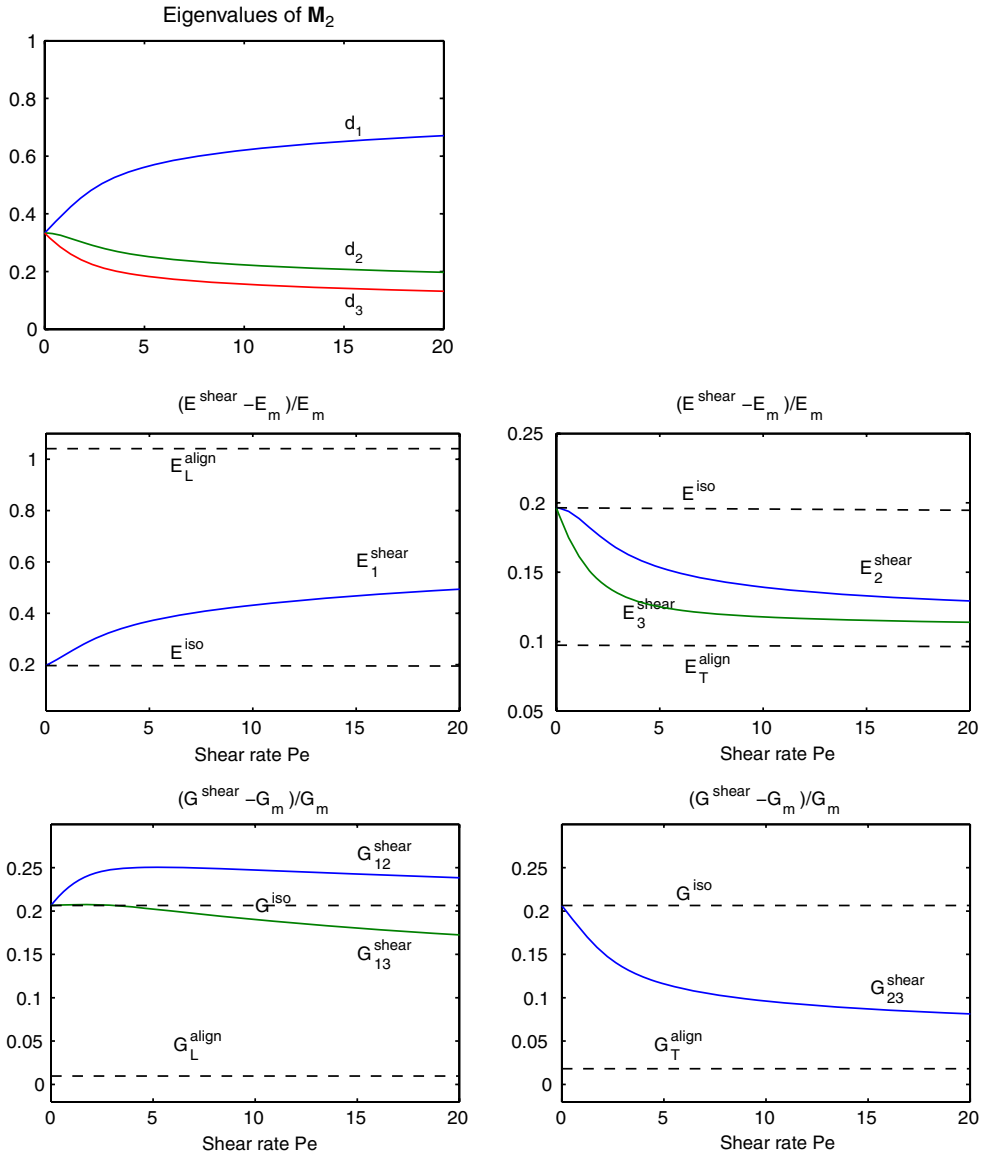

Fig. 2 Sheared PDFs and effective moduli for 1% volume fraction nano-rods of aspect ratio 100, with particle-matrix properties of Table 1 [24]. **a** Eigenvalues ($d_1 > d_2 > d_3$) of $\mathbf{M}_2$ versus normalized shear rate (Peclet number Pe); **b, c** relative enhancement of Young's moduli; **d, e** relative enhancement of shear moduli. *Dashed curves* correspond to perfectly aligned or random PDFs

- Longitudinal Young's modulus E_L^{exten} departs from E^{iso} and increases to the upper bound E_L^{align}: $E^{\text{iso}} < E_L^{\text{exten}} < E_L^{\text{align}}$ (Fig. 4b).
- Transverse Young's modulus E_T^{exten} decreases and appears to violate the often-assumed lower bound of the totally aligned PDF E_T^{align} (Fig. 4c).
- Longitudinal shear modulus G_L^{exten} is maximal at a moderate extension rate, and then decreases and approaches the lower bound G_L^{align}: $G_L^{\text{align}} < G_L^{\text{exten}} < G^{\text{iso}}$ (Fig. 4d.)
- Transverse shear modulus G_L^{exten} decreases with extension rate Pe, and converges to the lower bound G_T^{align} monotonically: $G_T^{\text{align}} < G_T^{\text{exten}} < G^{\text{iso}}$ (Fig. 4e).

Lastly, we consider uniaxial extension at a higher (nematic) volume fraction $\theta_2 = 2.3\%$. Fig. 5 shows the enhancement of elastic moduli of the corresponding PDFs. Fig. 5a shows $d_1 \gg d_2 = d_3$. The elastic moduli

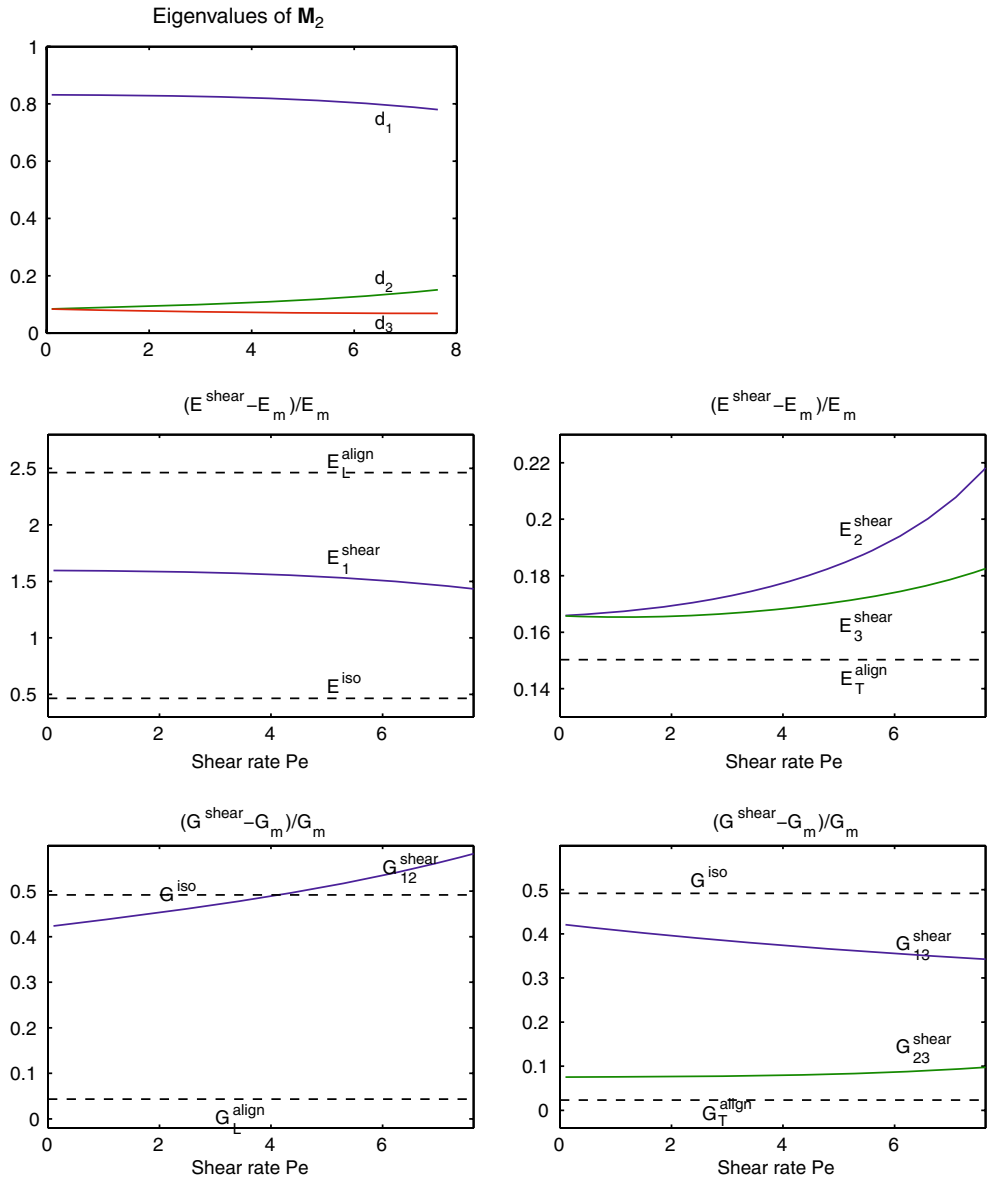

Fig. 3 Sheared PDFs and effective moduli for 2.3% volume fraction nano-rods of aspect ratio 100, arising from vorticity-aligned (logrolling) steady states. **a** Eigenvalues ($d_1 > d_2 > d_3$) of $\mathbf{M}_2$ versus normalized shear rate (Peclet number *Pe*); **b, c** relative enhancement of Young's moduli; **d, e** relative enhancement of shear moduli. *Dashed curves* correspond to perfectly aligned or random PDFs

show similar behavior to Fig. 4, except that the longitudinal shear modulus G_L^{exten} is strictly below the isotropic shear modulus G^{iso} and decreases with extension rate.

5 Conclusions

The micro-mechanics-based Mori–Tanaka method has been combined with the probability distribution functions (PDFs) of the Doi–Hess hydrodynamic theory for nano-rod dispersions to predict the effective elastic properties of rest and flow-induced phases of nano-rod composites. We first characterize symmetries of the effective elasticity tensor, which are inherited from the PDFs. We show C^e is: isotropic if the PDF is random; transversely isotropic if the PDF is uniaxial; orthotropic for biaxial PDFs generated by irrotational flow; monoclinic symmetric for in-plane PDFs generated by rotational flow; and maximally anisotropic if the PDF

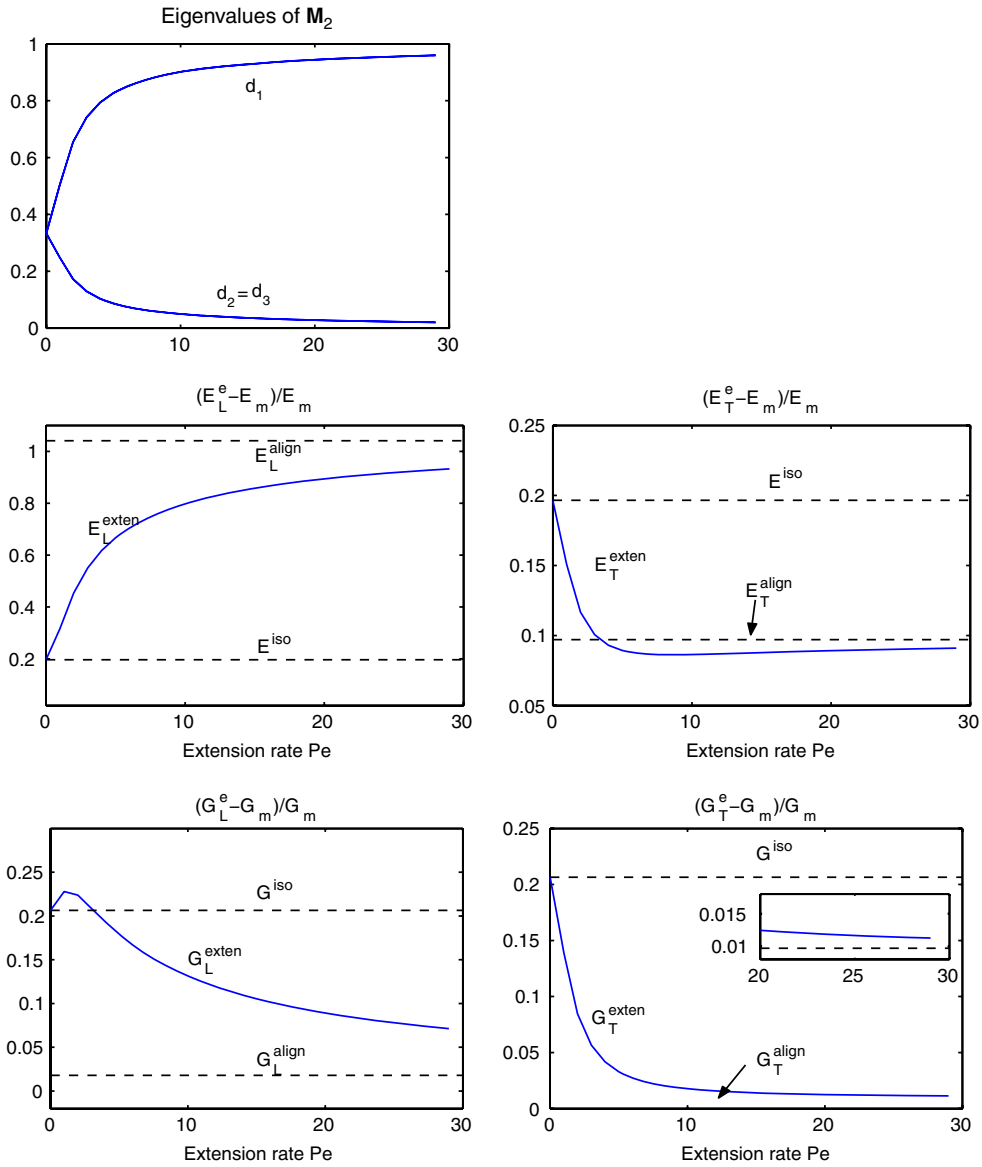

Fig. 4 Effective moduli for 1% volume fraction nano-rods of aspect ratio 100, arising from uniaxial extensional flow-induced PDFs. **a** Eigenvalues of $\mathbf{M}_2$ versus normalized extension rate *Pe*; **b** relative enhancement of longitudinal Young's moduli; **c** relative enhancement of transverse Young's moduli; **d** relative enhancement of longitudinal shear moduli. **e** relative enhancement of transverse shear moduli. *Dashed curves* correspond to perfectly aligned or random PDFs

is fully biaxial (typical of sheared ensembles). C^e is thereby determined to have 2, 5, 9, 13 or 21 independent components, which imply the composite has that number of independent elastic moduli, as volume fraction, flow type and rate vary.

Next, we implement the Mori–Tanaka formula for C^e using numerical databases for the PDFs of the Doi–Hess theory. For fixed aspect ratio, we compute the volume fraction dependence of the effective moduli for quiescent equilibrium distributions. The key feature is that moduli inherit not only symmetry from the PDF, but also bistability and hysteresis of the classical Onsager isotropic–nematic phase diagram. The trends of the various moduli are calculated versus volume fraction, exhibiting nonlinear gains of principal compressible (Young's) moduli and corresponding drops in transverse shear moduli. Next, the effects of flow rate on isotropic (low volume fraction) and nematic (high volume fraction) composites are detailed. All moduli of nano-rod ensembles are compared with those arising from nano-rod ensembles with random and perfect alignment. We

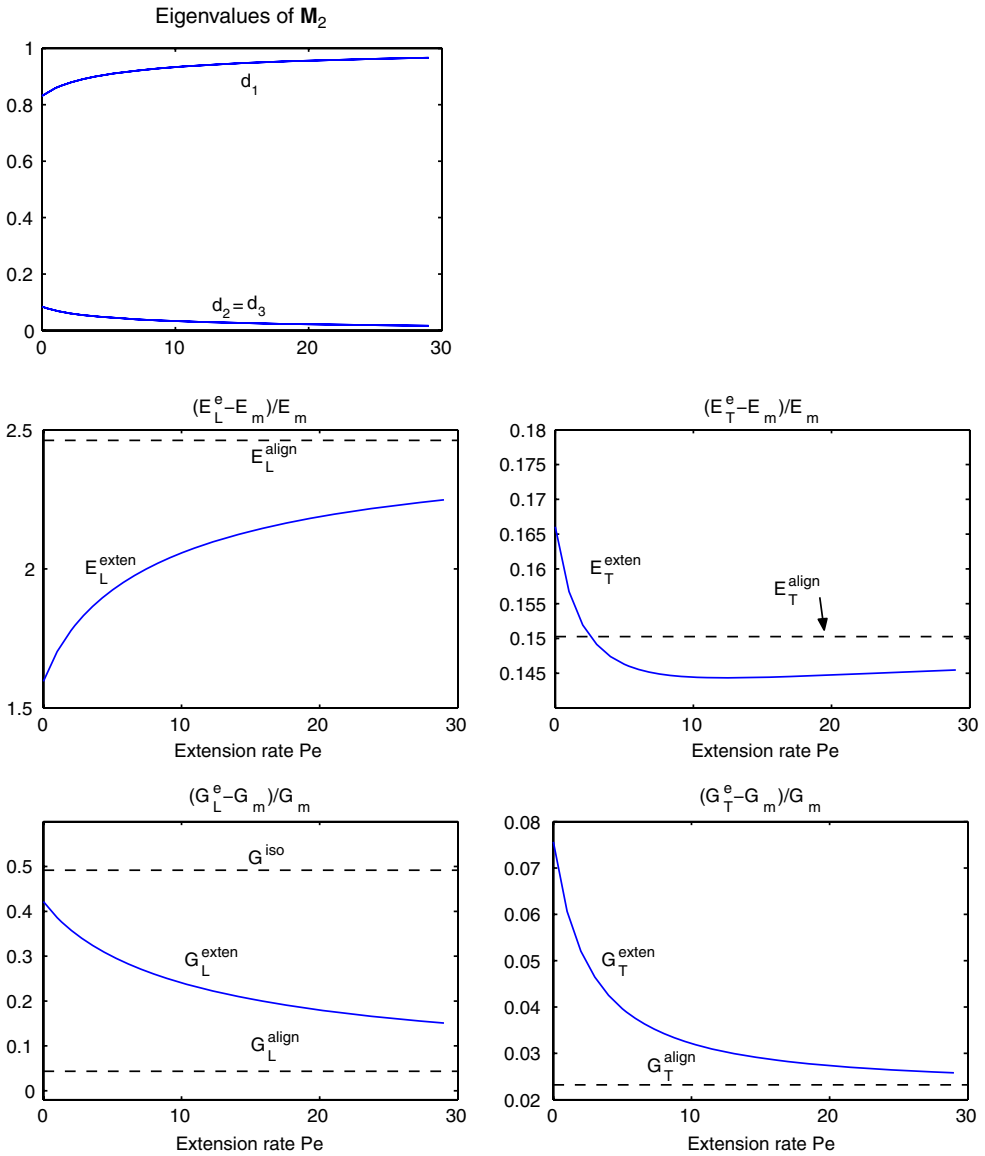

Fig. 5 Effective moduli for 2.3% volume fraction nano-rods of aspect ratio 100, arising from uniaxial extensional flow-induced PDFs. **a** Eigenvalues of $\mathbf{M}_2$ versus normalized extension rate *Pe*; **b** relative enhancement of longitudinal Young's moduli; **c** relative enhancement of transverse Young's moduli; **d** relative enhancement of longitudinal shear moduli; **e** relative enhancement of transverse shear moduli. *Dashed curves* correspond to perfectly aligned or random PDFs

find that shear moduli of quiescent and flow-induced nano-rod composites and Young's moduli of extensional flow-induced nano-rod composites are not bounded by the limit of random and perfectly aligned ensembles, whereas all other moduli do respect these bounds.

The natural extensions of this work are to dynamic PDFs in steady shear flow to assess mechanical moduli fluctuations, to the consideration of a third *interphase* between the rod and polymer, and to heterogeneous nano-composites. These topics are presently being studied.

Acknowledgments The authors express thanks to Dr. Richard Vaia, Materials Division at Wright Patterson Air Force Base, for valuable advice and suggestions in developing this research topic. Effort sponsored by the Air Force Office of Scientific Research, Air Force Materials Command, USAF, grants FA9550-05-1-0008 and FA9550-06-1-0063, the National Science Foundation, grants DMS-0308019, 0406374, 0604891, and the Army Research Office. This work is supported in part by NASA University Research, Engineering and Technology Institute on Bio Inspired Materials (BIMat) under award no. NCC-1-02037.

References

1. Constantin, P., Kevrekidis, I., Titi, E.S.: Asymptotic states of a Smoluchowski equation, Arch. Ration. Mech. Anal. **174**, 365–384 (2004)
2. Doi, M.: Molecular dynamics and rheological properties of concentrated solutions of rodlike polymers in isotropic and liquid crystalline phases. J. Polym. Sci. Polym. Phys. Ed. **19**, 229–243 (1981)
3. Doi, M., Edwards, S.F.: The theory of polymer dynamics. Oxford University Press, New York (1986)
4. Eshelby, J.D.: The determination of the elastic field of an ellipsoidal inclusion, and related problems. In: Proc. R. Soc. Lond., series A Math. Phys. Sci. **241**, 376–396 (1957)
5. Faraoni, V., Grosso, M., Crescitelli, S., Maffettone, P.L.: The rigid-rod model for nematic polymers: an analysis of the shear flow problem. J. Rheol. **43**, 829–843 (1999)
6. Forest, M.G., Zhou, H., Wang, Q.: Model study of the spinning of thermaotropic liquid crystalline polymers: fiber performance perdictions and bounds on throughput. Adv. Polym. Technol. **18**(4), 314–335 (1999)
7. Forest, M.G., Wang, Q., Zhou, H.: Homogeneous pattern selection and director instabilities of nematic liquid crystal polymers induced by elongational flows. Phys. Fluids **12**(3), 490–498 (2000)
8. Forest, M.G., Wang, Q., Zhou, R.: Symmetries of the Doi kinetic theory for nematic polymers of arbitrary aspect ratio: at rest and in linear flows. Phys. Rev. E **66**(3), 031712 (2002)
9. Forest, M.G., Wang, Q., Zhou, R.: The weak shear kinetic phase diagram for nematic polymers. Rheol. Acta **43**(1), 17–37 (2004a)
10. Forest, M.G., Wang, Q., Zhou, R.: The flow-phase diagram of Doi theory for sheared nematic polymers, II: finite shear rates. Rheol. Acta **44**(1), 80–93 (2004b)
11. Forest, M.G., Wang, Q., Zhou, R., Choate, E.: Monodomain response of arbitrary aspect ratio nematic polymers in general linear planar flows. J. Non-Newt. Fluid Mech. **118**(1), 17–31 (2004c)
12. Forest, M.G., Zheng, X., Zhou, R., Wang, Q., Lipton, R.: Anisotropy and dynamic ranges in effective properties of sheared nematic polymer nano-composites. Adv. Funct. Mater. **15**(12), 2029–2035 (2005)
13. Forest, M.G., Wang, Q., Zhou, R.: Extending the magnetic/electric field-hydrodynamic analogy of homogeneous rod and platelet liquid crystals and suspensions to strongly coupled fields. J. Rheol. (accepted 2006)
14. Forest, M.G., Sircar, S., Wang, Q., Zhou, R.: Monodomain dynamics for rigid rod and platelet suspensions in strongly coupled coplanar linear flow and magnetic fields II: kinetic theory. Phys. Fluids (accepted 2006)
15. de Gennes, P.G., Prost, J.: The physics of liquid crystals. Oxford University Press, New York (1993)
16. Gusev, A.A., Lusti, H.R.: Rational design of nanocomposites for barrier applications. Adv. Mater. **13**(21), 1641–1643 (2001)
17. Gusev, A., Lusti, H.R., Hine, P.J.: Stiffness and thermal expansion of short fiber composites with fully aligned fibers. Adv. Eng. Materials **4**(12), 927–931 (2002)
18. Hess, S.: Fokker–Planck-equation approach to flow alignment in liquid crystals. Z. Naturforsch **31A**(9), 1034–1037 (1976)
19. Hill, R.: Theory of mechanical properties of fiber-strengthened materials: I. Elastic behavior. J. Mech. Phys. Solids **12**, 199–212 (1964)
20. Lahiff, E., Leahy, R., Coleman, J.N., Blau, W.J.: Physical properties of novel free-standing polymer-nanotube thin films. Carbon **44**, 1525–1529 (2006)
21. Larson, R.G., Ottinger, H.: The effect of molecular elasticity on out-of-plane orientations in shearing flows of liquid crystalline polymers. Macromolecules **24**, 6270–6282 (1991)
22. McGee, S.H.: The influence of microstructure on the elastic properties of composite materials. Ph.D. Dissertation of the University of Delaware (1982)
23. Milton, G.W.: The Theory of Composites. Cambridge University Press, Cambridge (2002)
24. Odegard G.M., Gates T.S., Wise K.E., Park C., Siochi E.J.: Constitutive modeling of nanotube-reinforced polymer composites. Compos. Sci. Technol. **63**, 1671–1687 (2003)
25. Onsager, L.: The effects of shapes on the interaction of colloidal particles. Ann. N.Y. Acad. Sci. **51**, 627 (1949)
26. Qiu, Y.P., Weng, G.J.: On the application of Mori–Tanaka's theory involving transversely isotropic spheroidal inclusions. Int. J. Eng. Sci. **28**, 1121–1137 (1990)
27. Song, W., Kinloch, I.A., Windle, A.H.: Nematic liquid crystallinity of multiwall carbon nanotubes. Science **302**, 1363 (2003)
28. Torquato, S.: Random heterogeneous materials. Springer, Berlin Heidelberg New York (2002)
29. Vaia R.A.: Polymer Nanocomposites. Oxford University Press, New York (2002)
30. Walpole, L.J.: On the overall elastic moduli of composite materials. J. Mech. Phys. Solids **17**, 235–251 (1969)
31. Zheng, X., Forest, M.G., Lipton, R., Zhou, R., Wang, Q.: Exact scaling laws for electrical conductivity properties of nematic polymer nano-composite monodomains. Adv. Funct. Mater. **15**(4), 627–638 (2005)